PHYSICAL REVIEW B **90**, 125303 (2014)

Capacitative coupling of singlet-triplet qubits in different interqubit geometries

Tuukka Hiltunen and Ari Harju
Department of Applied Physics, Aalto University School of Science, P.O. Box 14100, 00076 Aalto, Finland

(Received 17 April 2014; revised manuscript received 28 August 2014; published 5 September 2014)

In the singlet-triplet qubit architecture, the two-qubit interactions required in universal quantum computing can be implemented by capacitative coupling, by exploiting the charge distribution differences of the singlet and triplet states. The efficiency of this scheme is limited by decoherence, that can be mitigated by stronger coupling between the qubits. In this paper, we study the capacitative coupling of singlet-triplet qubits in different geometries of the two-qubit system. The effects of the qubit-qubit distance and the relative orientation of the qubits on the capacitative coupling strength are discussed using an accurate microscopic model and exact diagonalization of it. We find that trapezoidal quantum dot formations allow strong coupling with low charge distribution differences between the singlet and triplet states. The analysis of geometry on the capacitative coupling is also extended to the many-qubit case and the creation of cluster states.

DOI: 10.1103/PhysRevB.90.125303 PACS number(s): 73.22.−f, 81.07.Ta

I. INTRODUCTION

Two-electron spin eigenstates in semiconductor double quantum dots (DQD) were proposed as qubits [1] by Levy in 2002 [2] and allow a scalable architecture for quantum computation [3]. The universal set of quantum gates for two spin singlet-triplet DQD qubits has been demonstrated experimentally [4–6]. In this architecture, the two-qubit operations required for universality are implemented using long-distance capacitative coupling by the Coulomb interaction, in which the charge asymmetries of the singlet and triplet states are exploited [3,6,7]. The capacitative coupling of singlet-triplet qubits, resulting in a two-qubit CPHASE-gate, has been achieved in experiments [6].

The capacitative two-qubit operation can be used to create a maximally entangled Bell state between singlet-triplet qubits. Entanglement is an essential resource in quantum information technology and it is at the heart of all quantum computing [8]. Coupling more than two qubits together allows the generation of multipartite entangled states, including the Greenberger-Horne-Zeilinger (GHZ) [9–11] and cluster states [12,13]. These highly entangled states have applications for example in the proposed one-way quantum computer [14,15], an alternative to the circuit model of quantum computing [16].

In implementing the qubit operations, the coupling between the quantum dot and the semiconductor environment leads to a common problem in quantum computing, namely decoherence. The most important electron spin decoherence sources considering singlet-triplet qubits are the coupling to the nuclear spins in host materials such as GaAs [17–20] and the effects of the fluctuating charge environment [21–23]. In the experimental realizations of quantum gate operations, the effects of decoherence can be minimized by decreasing the gate operation times. In the case of the two-qubit capacitative gate, this can be achieved by enhancing the qubit-qubit coupling. Stronger coupling also allows the use of smaller charge asymmetries that are less susceptible to the charge noise [23–26].

In this paper, we model the capacitative coupling of singlet-triplet qubits using accurate exact diagonalization (ED) techniques. We study different qubit geometries and find that the ones allowing stronger couplings and hence more efficient quantum gate architectures are those in which the quantum dots of the qubits form a trapezoid. We also find certain "dead angles" geometries, in which the capacitative coupling disappears completely. The analysis on the effects of qubit-qubit geometry is also extended to the many-qubit case, where we use an accurate microscopic model to simulate the creation of cluster states between singlet-triplet qubits.

This paper is organized as follows. In Sec. II, we discuss the computational methods and the simulation model used in the paper. Section III is devoted to the analysis of the two-qubit coupling. We study the effects of the distance of the qubits and their relative orientation on the strength of the capacitative coupling and the entangling properties of the two-qubit gate. We find the geometries yielding strong qubit-qubit coupling and analyze the two-qubit gate operation in different coupling geometries. In Sec. IV, we simulate the creation of cluster states by CPHASE operations between adjacent qubits.

II. MODEL AND METHODS

A. Continuum model

A lateral GaAs quantum dot system with N electrons is described with the Hamiltonian

$$H = \sum_{j=1}^{N}\left[-\frac{\hbar^2}{2m^*}\nabla_j^2 + V(\mathbf{r}_j,t)\right] + \sum_{j<k}\frac{e^2}{4\pi\epsilon r_{jk}}, \quad (1)$$

where $m^* = 0.067\,m_e$ and $\epsilon = 12.7\,\epsilon_0$ are the effective electron mass and permittivity in GaAs, respectively. The external potential $V(\mathbf{r})$ for quantum dot systems is approximated with a piecewise parabolic potential that consists of several parabolic wells. A confinement potential of n parabolic wells can be written as

$$V(\mathbf{r}) = \tfrac{1}{2}m^*\omega_0^2 \min_{1\leqslant m\leqslant n}\{|\mathbf{r}-\mathbf{R}_m|^2\} + V_d(t,\mathbf{r}), \quad (2)$$

where $\{\mathbf{R}_m\}_{1\leqslant m\leqslant n}$ are the locations of the minima of the parabolic dots, and ω_0 is the confinement strength. A time-dependent detuning potential $V_d(t,\mathbf{r})$ is included.

In our ED computations, the electrostatic detuning between the two minima of a DQD system is modeled as a step function that assumes constant values at each dot. The discontinuity in the detuning potential is found to have no effects compared to the continuous case of our previous study [27]. The detuning of a singlet-triplet qubit is defined as the potential energy difference between the two parabolic minima of the qubit; i.e., if the qubit consists of parabolic wells at $\mathbf{R}_1$ and $\mathbf{R}_2$, the detuning is given as $\epsilon(t) = V(\mathbf{R}_1,t) - V(\mathbf{R}_2,t)$.

B. Lattice model

Although accurate, the continuum model ED is computationally very expensive and thus limited to small particle numbers (no more than two $S-T_0$ qubits can be modeled accurately) and a full scanning of various QD system geometries is not possible. A more flexible method for studying systems of several $S-T_0$ qubits is the extended Hubbard model with the inclusion of a long-range Coulomb interaction.

In this model, a system consisting of N_q singlet-triplet qubits ($N = 2N_q$ electrons and QDs) can be described using the Hamiltonian

$$H = \sum_{i\sigma} E_{i\sigma} a^\dagger_{i\sigma} a_{i\sigma} - \sum_{ij\sigma} t_{ij\sigma} a^\dagger_{i\sigma} a_{j\sigma} + U \sum_i n_{i\downarrow} n_{i\uparrow} + \sum_{\sigma\sigma'} \sum_{i<j} U_{ij} n_{i\sigma} n_{j\sigma'}. \qquad (3)$$

Here, i and j are the site indices, and σ and σ' the spin indices. $E_{i\sigma}$ are the on-site energies at each QD, $t_{ij\sigma}$ the tunneling element between dots, and U the on-site Coulomb repulsion. U_{ij} is the long-range Coulomb interaction between sites i and j, and $n_{i\sigma}$ the charge at site i with the spin σ. In this paper, the tunneling $t_{ij\sigma} = t_{ij}$ is nonzero only between the adjacent dots inside a qubit (i.e., there is no tunneling between the qubits). The long-range electron-electron interaction is given as

$$U_{ij} = \frac{C}{|\mathbf{r}_i - \mathbf{r}_j| - \eta}, \qquad (4)$$

where $C = e^2/4\pi\epsilon$ is the Coulomb-strength, and $\mathbf{r}_i$ and $\mathbf{r}_j$ are the locations of the dots i and j. $\eta > 0$ is an extra constant conveying the fact that in reality the wave functions have finite widths. The parameters of the Hubbard model (U, t_{ij}, and η) can be fitted to continuum model data in order to produce more realistic results.

C. Computational methods

The continuum Hamiltonian (1) is diagonalized using the ED method. In the ED many-body calculations, the one-particle basis is the eigenstates corresponding to the confinement potential (2). The multiparticle basis, in which the Hamiltonian of Eq. (1) is diagonalized, is constructed from the single-particle eigenstates as the antisymmetrized Fock states. The one-particle eigenstates $\{|\psi_p\rangle\}_{p=1}^{N_1}$ (the eigenbasis size being N_1) are computed using the multicenter Gaussian basis $\{|\phi_i\rangle\}_{i=1}^{N_g}$ (the method is described in detail by Nielsen *et al.* [26]). The Coulomb-interaction matrix elements $V_{i,j,k,l} = \langle\phi_i|\langle\phi_j|1/|\mathbf{r}_1 - \mathbf{r}_2||\phi_l\rangle|\phi_k\rangle$ can be computed analytically in the Gaussian basis. The elements $V_{i,j} = \langle\phi_i|V(\mathbf{r})|\phi_j\rangle$ can also be computed analytically for certain confinement potentials $V(\mathbf{r})$, but generally they must be obtained using numerical integration. The matrix elements $\tilde{V}_{p,q}$ and $\tilde{V}_{p,q,r,s}$ corresponding to the one-particle eigenstates are then computed from the Gaussian elements by basis changes, as $\tilde{V}_{p,q} = \sum_{i,j}\langle\psi_s|\phi_i\rangle\langle\phi_j|\psi_q\rangle V_{i,j}$ and $\tilde{V}_{p,q,r,s} = \sum_{i,j,k,l}\langle\psi_p|\phi_i\rangle\langle\psi_q|\phi_j\rangle\langle\phi_k|\psi_r\rangle\langle\phi_l|\psi_s\rangle V_{i,j,k,l}$ (the sums go from 1 to N_g).

In the computation of the one-particle eigenstates, $\{|\psi_p\rangle\}_{p=1}^{N_1}$, an evenly spaced grid of several hundred Gaussian functions (up to $N_g = 500$) is used. The grid dimensions and the Gaussian widths are optimized and the convergence of the states is verified by comparing the energies to ones obtained with a much larger grid. We perform the basis change corresponding to the elements $\tilde{V}_{p,q,r,s}$ with an Nvidia Tesla C2070 graphics processing unit which was programmed with CUDA [28], a parallel programming model for Nvidia GPUs. The many-body eigenstates are computed with ED using 18 first single-particle states ($N_1 = 18$). This basis size is found to be sufficient for the convergence of the results (the relative difference of the many-body ground-state energies with 18 and 24 single-particle states is less than 0.1% up to very high detuning region).

The continuum Hamiltonian is diagonalized using the Lanczos algorithm for sparse matrices. In the Lanczos method, only the ground state and its energy are obtained accurately. The higher lying eigenstates can be obtained using a "ladder operation." The kth state $|\psi_k\rangle$ is obtained as the ground state of the Hamiltonian

$$H_k = H + \delta \sum_{s=1}^{k-1} |\psi_s\rangle\langle\psi_s|, \qquad (5)$$

where H is the original Hamiltonian of the system and $\delta > 0$ is a penalizing constant that moves the lower eigenstates $\{|\psi\rangle_s\}_{s=1}^{k-1}$ above the desired kth state. The lattice Hamiltonian of Eq. (3) can be diagonalized directly, as its linear dimensions do not exceed 100 in the computations done in this study.

The time evolution of a $S-T_0$ qubit system, described by the wave function $|\psi(t)\rangle$ and governed by the Hamiltonian $H(t)$, is computed by propagation,

$$|\Psi(t+\Delta t)\rangle = \exp\left[-i\Delta t H(t)/\hbar\right]|\Psi(t)\rangle. \qquad (6)$$

Here, t and Δt are time and time step length, respectively. $H(t)$ is either the lattice or the continuum Hamiltonian. In the continuum case, the exponential is computed using the Lanczos method.

III. TWO CAPACITATIVELY COUPLED QUBITS

In the capacitative coupling of singlet-triplet qubits, the interqubit operations are achieved by exploiting the differences of the charge distributions of the singlet and triplet states under exchange interaction. With nonzero exchange, achieved by electrically detuning the qubits, the singlet state localizes more into the dot with lower potential; i.e., the lowest singlet state is a superposition of the symmetric charge state $|S(1,1)\rangle$ and the localized charge state $|S(0,2)\rangle$. The triplet, however, stays in the (1,1) charge configuration due to its spatially antisymmetric wave function. As the singlet and triplet states have different charge distributions, the Coulomb repulsion between two neighboring qubits depends on their states. This creates an entangling two-qubit CPHASE gate when two qubits are detuned simultaneously towards the $|S(0,2)\rangle$ regime.

The strongest coupling is achieved when the two qubits A and B are initiated in the xy plane of the Bloch sphere, and then evolved under exchange, causing them to entangle. The entanglement can be characterized by an entanglement measure, such as concurrence [8]. Concurrence C assumes values between 0 and 1, and the bigger the value, the stronger the entanglement.

A formula for the evolution of the concurrence by capacitative coupling of two $S - T_0$ qubits can be derived by writing the Hamiltonian in the two-qubit basis $\{|SS\rangle, |ST_0\rangle, |T_0S\rangle, |T_0T_0\rangle\}$, which results in a diagonal matrix with the energies of the aforementioned qubit basis states as its diagonal entries. In this basis, the two-qubit wave function is written as $|\Psi(t)\rangle = \sum_{X=S,T_0} \sum_{Y=S,T_0} \alpha_{XY}(t)|XY\rangle$, and at $t = 0$ all coefficients $\alpha_{XY} = 1/2$ as the qubits are initiated in the xy plane. In the time evolution of the system, each of the four terms obtains a phase factor corresponding to its energy. Defining a 2×2-matrix, $\mathbf{M}(t)$, so that $M_{11}(t) = \alpha_{SS}(t)$, $M_{22}(t) = \alpha_{T_0T_0}(t)$, $M_{12}(t) = \alpha_{ST_0}(t)$, and $M_{21}(t) = \alpha_{T_0S}(t)$, the concurrence is given as $C(t) = 2|\det(\mathbf{M})|$ [8], yielding

$$C(t) = \tfrac{1}{2}\sqrt{2 - 2\cos\left(E_{cc}t/\hbar\right)}, \tag{7}$$

with the differential cross capacitance energy between the two double-dot systems,

$$E_{cc} = |E_{SS} + E_{T_0T_0} - E_{ST_0} - E_{T_0S}|. \tag{8}$$

Here, E_{SS} is the energy of the qubit basis state $|SS\rangle = |S\rangle_A \otimes |S\rangle_B$, and similarly for the other terms. E_{cc} determines the speed of the gate operation and the frequency of the entanglement oscillations. At time t when $tE_{cc}/\hbar$ is an odd multiple of π, $C(t) = 1$ and the maximal Bell-state entanglement is achieved.

The physics of a system of two capacitatively coupled $S - T_0$ qubits (apart from the decoherence effects [18,19,22]) depend essentially on two things, the intraqubit tunneling (the tunneling between the two dots of the qubit) and the Coulomb repulsion between the qubits, i.e., how the two qubits are located with respect to each other. The tunneling strength controls the anti-crossing energy gap of the singlet charge states $|S(1,1)\rangle$ and $|S(0,2)\rangle$. The locations and distance of the qubits affect both the energy differences of the charge states and the locations of the anticrossing, i.e., the detuning required for the singlet transition from (1,1) to (0,2).

The topic of this section is the study of the effect of the geometry of the two-qubit system on the capacitative coupling strength and the entangling properties of the gate. An illustration of the dot locations in a two-qubit system is shown in Fig. 1. In this system, the confinement strength is set to $\hbar\omega_0 = 4$ meV and the intraqubit dot distance is $|\mathbf{R}_1 - \mathbf{R}_2| = |\mathbf{R}_3 - \mathbf{R}_4| = 80$ nm. The geometry of this two-qubit system is defined by the angles α and β and the interqubit distance d.

When modeling the qubits with piecewise parabolical potentials, the intraqubit tunneling is determined by the distance and the confinement strengths of the parabolic wells. In order for the qubit to function properly, the tunneling barrier between the dots has to be high enough that with zero detuning the singlet and triplet states are approximately degenerate; i.e., the exchange can be set to a very small value. This sets lower bounds for viable confinement strengths and intraqubit dot distances. Changing the intraqubit tunneling does not have a large effect on the capacitative coupling that is governed by the interqubit Coulomb repulsion.

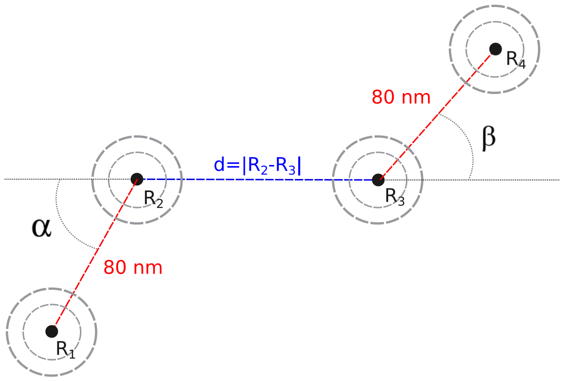

FIG. 1. (Color online) Locations of the QDs of a two-qubit system. Qubit A consists of dots at $\mathbf{R}_1$ and $\mathbf{R}_2$ and B of those at $\mathbf{R}_3$ and $\mathbf{R}_4$. The qubit-qubit distance is $d = |\mathbf{R}_2 - \mathbf{R}_3|$. The confinement strength is $\hbar\omega_0 = 4$ meV and the intraqubit dot distance is 80 nm. The angles α and β determine the locations of dots 1 and 4.

The locations of the qubits have a quite complex effect on the behavior of the two-qubit gate. For example, the Coulomb repulsion can either facilitate or inhibit the charge transitions to $|S(0,2)\rangle$, depending on the locations of the low-detuned dots in the two qubits. If the farthest away dots are detuned to low potential, the transition to (0,2) can happen with lower detuning as it decreases the repulsion between the qubits. Next, we are going to study the behavior of the two-qubit system with several different interqubit geometries. The results shown and discussed in this section are obtained using the continuum model unless stated otherwise. We will discuss the contributions of the qubit-qubit distance (d in Fig. 1) and qubit orientations (α and β in Fig. 1) separately.

A. Linear alignment of qubits

In the simplest case, both qubits, i.e., all four QDs, are located in a straight line (corresponding to $\alpha = \beta = 0$ in Fig. 1). We study the effect of the qubit-qubit distance $d = |\mathbf{R}_2 - \mathbf{R}_3|$. The farthest away dots at $\mathbf{R}_1$ and $\mathbf{R}_4$ are detuned to low potential. The energies of the lowest eigenstates are computed as a function of the detunings $\epsilon_A = V(\mathbf{R}_2) - V(\mathbf{R}_1) = \epsilon_B = V(\mathbf{R}_3) - V(\mathbf{R}_4) = \epsilon$. The energies with $d = 100$ nm are shown in the upper left and the energies with $d = 160$ nm in the upper right plot of Fig. 2.

The figures show the anticrossing region of the $|S(1,1)\rangle$ and $|S(0,2)\rangle$ states. When the detuning overcomes the repulsion of two electrons occupying one QD, the ground-state singlet shifts from (1,1) to (0,2). In addition to the $|S(0,2)\rangle_A \otimes |S(0,2)\rangle_B$ and $|S(1,1)\rangle_A \otimes |S(1,1)\rangle_B$ labeled in the figures, there are also two other $|SS\rangle$-type states [the two blue middle curves besides the $S(0,2)S(0,2)$ and $S(1,1)S(1,1)$], namely “the bonding state” and “the antibonding state,”

$$\frac{1}{\sqrt{2}}|S(1,1)\rangle_A \otimes |S(0,2)\rangle_B \pm \frac{1}{\sqrt{2}}|S(0,2)\rangle_A \otimes |S(1,1)\rangle_B,$$

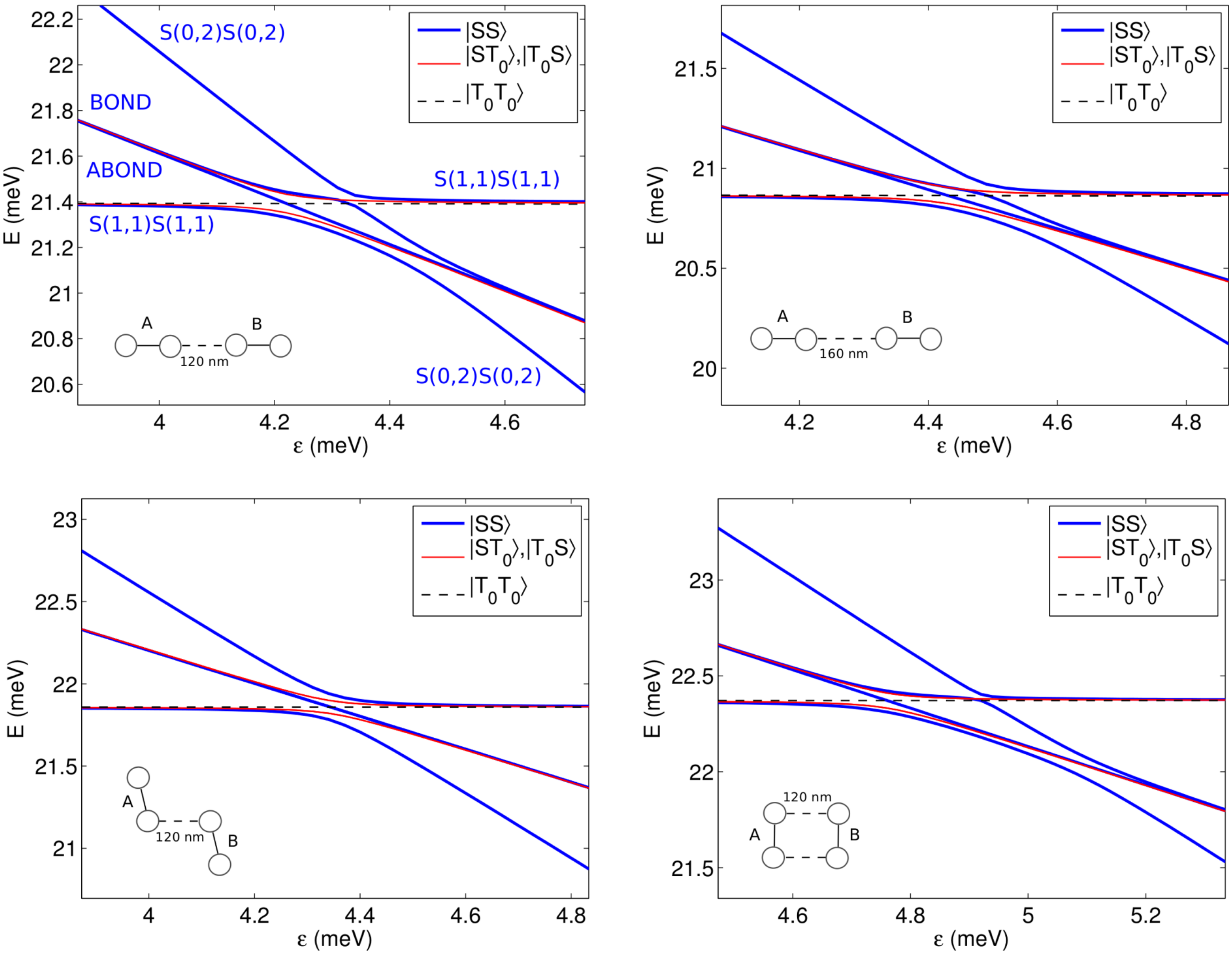

FIG. 2. (Color online) The energy levels of the two-qubit system as a function of the detuning (see Fig. 1 for the illustration of the system). Both qubits are in the same detuning $\epsilon_A = \epsilon_B = \epsilon$. The $|SS\rangle$ states are shown with the thick blue lines, the $|ST_0\rangle$ and $|T_0S\rangle$ states with the red lines, and the $|T_0T_0\rangle$ state with the dashed black line. Illustrations of the corresponding QD formations are shown on top of the plots. Upper left: ($\alpha = \beta = 0$) with the qubit-qubit distance $d = 120$ nm. The different singlet-charge states are denoted with labels. Upper right: Linearly aligned system with $d = 160$ nm. Lower left: A “dead angles” case $\alpha = \beta = 0.4534\pi$ with $d = 120$ nm. Lower right: Rectangular qubit formation ($\alpha = -\beta = 0.5\pi$) with $d = 120$ nm.

where $+$ corresponds to the bonding state and $-$ to the antibonding state. The energy eigenstates of a similar two-qubit system are discussed with more detail in our previous work [27], including cases with asymmetric detuning, $\epsilon_1 \neq \epsilon_2$.

When the farthest away dots 1 and 2 are detuned to low potential, i.e., when $\epsilon_A,\epsilon_B > 0$, the Coulomb repulsion caused by the other qubit facilitates the transition to (0,2); it is preferable for the electrons of qubit A to be as far as possible from qubit B. The shorter the qubit-qubit distance d the larger this effect is. This is evident from the figures. In the upper left plot of Fig. 2, the anticrossing region starts around $\epsilon = 3.9$ meV, and in the upper right one around $\epsilon = 4.2$ meV. In the $d = 100$ nm case, the eigenenergies are higher due to the larger repulsion. The energy differences of the qubit states $\{|SS\rangle,|ST_0\rangle,|T_0S\rangle,|T_0T_0\rangle\}$ are also affected, and the width of the anticrossing region increases as the Coulomb repulsion becomes more prominent. If the closer dots 1 and 2 are instead detuned to low potential (i.e., $\epsilon_A < 0$ and $\epsilon_B < 0$), the anticrossing region will shift to higher detuning values, but otherwise the behavior of the two-qubit system stays similar.

The values of E_{cc} [Eq. (8)] as a function of the detunings ϵ with several different qubit-qubit distances are shown in Fig. 3. The value of E_{cc} starts to increase when the detuning has reached the anticrossing area, saturating to a constant value when the singlet is fully in (0,2) [it stays constant until the triplet also starts to undergo the transition to (0,2) at much higher detuning]. The shorter the qubit-qubit distance, the larger the maximal value of E_{cc} is, as with shorter distances the Coulomb repulsion between the qubits has more contribution in the energies of the qubit states.

B. Rotated qubits

Next, we discuss the effect of the orientation of the qubits while keeping the qubit-qubit distance constant. The qubits were set $d = |\mathbf{R}_2 - \mathbf{R}_3| = 120$ nm apart from each other,

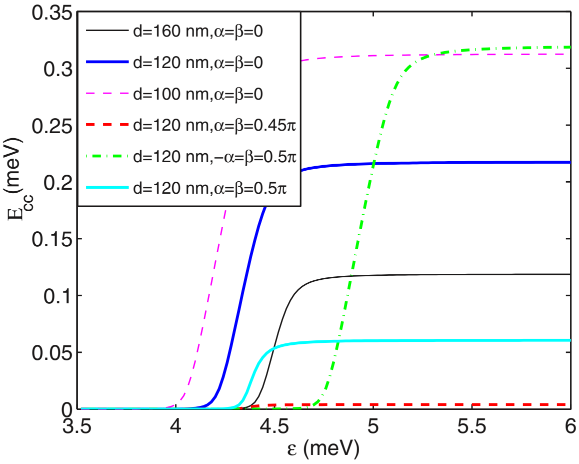

FIG. 3. (Color online) The values of the cross capacitance $E_{cc} = |E_{SS} + E_{T_0T_0} - E_{ST_0} - E_{T_0S}|$ as a function of the detunings $\epsilon_A = \epsilon_B = \epsilon$ with several different values of the qubit-qubit distance $d = |\mathbf{R}_2 - \mathbf{R}_3|$ and angles α and β (see Fig. 1).

with the intraqubit dot distance being 80 nm. The locations of the farthest away dots (again detuned to low potential) were varied. An illustration of the system can be seen in Fig. 1. Probing the different values of the angles α and β in Fig. 1 would be very cumbersome using the continuum model. In order to avoid having to compute new sets of one-particle eigenstates corresponding to each dot configuration, we study the angle dependence using the Hubbard model of Eq. (3) with its parameters t_{ij}, U, and η fitted to the continuum model data.

In the case of a reference system of two $S - T_0$ qubits with the qubit-qubit distance 120 nm, intraqubit distance 80 nm, confinement strength $\hbar\omega_0 = 4$ meV, and linear alignment, a good fit is obtained with $t_{ij} = 27.8$ μeV, $U = 3.472$ meV, and $\eta = 0.43$ nm. The parameter fit is demonstrated in the left panel of Fig. 4. The figure shows lowest energies of the two-qubit system (see Fig. 1 for an illustration of the geometry of the two-qubit system) as functions of the detunings of the qubits, $\epsilon_A = \epsilon_B = \epsilon$. As seen in the figure, the fitted energies coincide with the continuum model ones. The fit is also tested with asymmetric detunings, $\epsilon_A \neq \epsilon_B$, and is found equally good in that case. As the capacitative coupling of singlet-triplet is governed by the energy differences of the qubit states, the Hubbard model with the fitted parameters can be used to accurately describe the coupling.

If the geometry of the system (i.e., the dot distances, locations, and confinements) is changed, generally a new fit for the parameters has to be computed. However, if the dot distances and the confinement are kept the same and only the qubit orientations (i.e., the angles α and β in Fig. 1) are changed the same fit is found to agree well. The right panel of Fig. 4 shows the energies of a system with $\alpha = \beta = 0.4534\pi$. The Hubbard parameters correspond to the fit with $\alpha = \beta = 0$, i.e., the same parameters used in the left panel of Fig. 4. As seen in the figure, the energies differ now a bit more compared to left panel but the fit can still be considered good. The Hubbard model can thus be used to probe the values of α and β while keeping the qubit-qubit distance constant (a task that would be very cumbersome using the continuum model).

The maximum value of E_{cc} as a function of the angles α and β is shown in Fig. 5. The figure is obtained by using the Hubbard model of Eq. (3) with the parameters obtained in the fit in Fig. 4. In Fig. 5, the detuning is symmetrical, $\epsilon_A = \epsilon_B$, but the orientations resulting in high coupling apply for the general case as well; i.e., the angle dependence of E_{cc} is similar also to asymmetric detunings, such as $\epsilon_A = -\epsilon_B$. Figure 3 shows the E_{cc} values as functions of the detunings ϵ with several different angles.

As seen in Fig. 5, $E_{cc}^{\max}$ obtains its largest values along the line $\alpha = -\beta$ that corresponds to the geometries in which the QDs of the system form a trapezoid. The $E_{cc}^{\max}$ values start to increase rapidly when the angles approach the rectangular formation at $\alpha = \pi/2$ and $\beta = -\pi/2$ and with $E_{cc}^{\max} = 0.3186$ meV. The qubit state energies in this case are

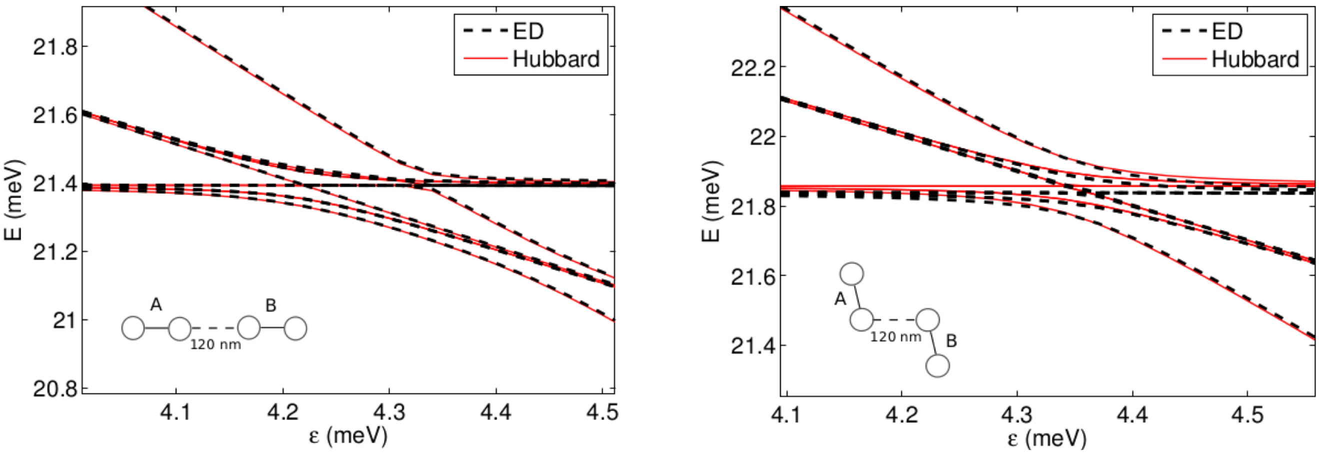

FIG. 4. (Color online) The lowest energies of a two-qubit system as function of the detunings $\epsilon_A = \epsilon_B = \epsilon$. The thick black dashed line shows the continuum ED energies, and the red line the Hubbard energies with the parameters $t_{ij} = 27.8$ μeV, $U = 3.472$ meV, and $\eta = 0.43$ nm. These parameters have been obtained by fitting the Hubbard energies to continuum data corresponding to $\hbar\omega_0 = 4$ meV confinement, 80 intraqubit dot distance, 120 nm qubit-qubit distance, and linear alignment ($\alpha = \beta = 0$ in Fig. 1). The energies of the fitted case are shown in the left panel. The right panel shows the continuum ED and Hubbard energies in the system with $\alpha = \beta = 0.4534\pi$ (see Fig. 1). The Hubbard parameters are the same as in the left panel; i.e., they are fitted to the $\alpha = \beta = 0$ case.

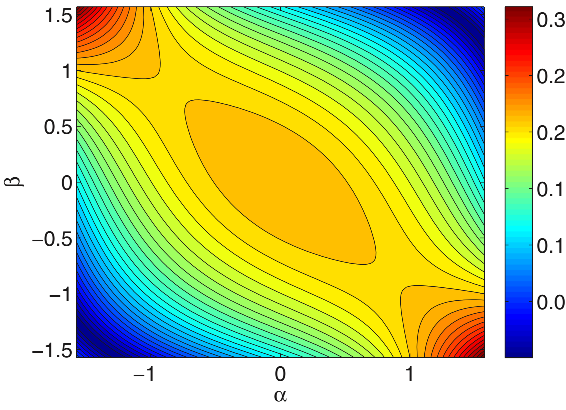

FIG. 5. (Color online) The maximum value $E_{cc}^{\max}$ of the differential cross capacitance energy E_{cc} as a function of the angles α and β (see Fig. 1 for the description of the system). The $E_{cc}^{\max}$ values are shown in meV. The values are computed using the extended Hubbard model with its parameters fitted to the continuum model data.

shown in the lower right plot of Fig. 2. If the angles are further increased in this direction, the values keep rising but in this case the qubit-qubit distance becomes smaller than 120 nm.

Along the line $\alpha = \beta$, the values of $E_{cc}^{\max}$ decrease as the angles are increased. Near $\alpha = \beta = \pi/2$, the maximum value has decreased to zero. For example, with $\alpha = \beta = 0.4534\pi$ the maximum value is $E_{cc}^{\max} = 1.7648 \times 10^{-10}$ meV compared to the $\alpha = \beta = 0$ value $E_{cc}^{\max} = 0.2159$ meV. With these "dead angles," the energy difference $E_{SS} + E_{T_0T_0} - E_{ST_0} - E_{T_0S}$ vanishes and E_{cc} is uniformly zero. The qubit state energies for the dead angle case $\alpha = \beta = 0.4354\pi$ are shown in the lower left plot of Fig. 2. Comparing this to the other plots of the figure, the anticrossing area width is smaller, and the intermediate bonding and antibonding $|SS\rangle$ states are completely degenerate. As the angles are then further increased, the values of E_{cc} start to rise again reaching $E_{cc}^{\max} =$ 0.06 meV at $\alpha = \beta = \pi/2$. Figure 3 shows the E_{cc} values in the rectangular case $-\alpha = \beta = 0.5\pi$, with $\alpha = \beta = 0.45\pi$ (close to the dead angle case), and with $\alpha = \beta = \pi/2$.

It should be noted that the behavior of the $E_{cc}^{\max}$ as a function of the angles α and β or the qubit distance d can be explained electrostatically. E_{cc} obtains its maximum values when the singlet is fully in the (0,2) configuration. Computing the value of $E_{cc}^{\max}$ according to Eq. (8) so that the singlet consists of two unit charges located at a single dot, and the triplet of one charge per dot, yields the same angle dependence that is seen in Fig. 5.

The strength of the qubit-qubit coupling, the energy difference E_{cc}, is observable by looking at the energies of the two-qubit systems. The energy difference between the intermediate bonding and antibonding states (the width of the "middle bulges" in Fig. 2) determines the strength of the capacitative coupling. In the cases where the bonding and antibonding states are close to degenerate [a small "bulge" as in Figs. 2(b) and 2(c)], E_{cc} assumes very small values, and the qubits are only weakly coupled.

C. Gate operation

In implementing the capacitative CPHASE gate, the strongly coupled geometries are preferable. Long gate operation times mean more errors due to decoherence from for example the charge noise [6,22,24]. In order to achieve fast enough gate operation in the weakly coupled cases, one needs larger charge distribution differences between the singlet and triplet states. Charge-noise-induced decoherence, an important error source in $S - T_0$ qubits, is increased considerably when the qubits are operated close to the (0,2) regime [3,22,24]. It should be noted that there have also been theoretical studies on additional effects beside the charge asymmetry, so called sweet spots in capacitative coupling of $S - T_0$, that can minimize the charge noise coupling (e.g., Refs. [25,29]).

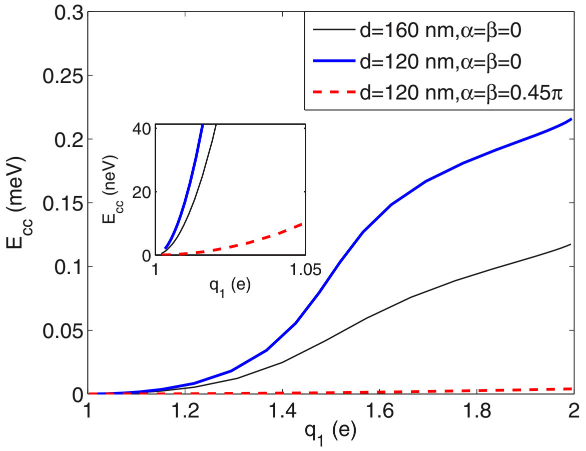

FIG. 6. (Color online) The cross capacitance E_{cc} values as a function of the charge in the low detuned dot 1 of qubit A, q_1 (the charge in the low detuned dot 4 of qubit B is exactly the same due to symmetry). The inset shows at the small E_{cc} region relevant to the CPHASE-gate operation time of tens of nanoseconds.

Figure 6 shows the fact that with weak coupling one needs large charge asymmetries in order to achieve fast operation. Figure 6 shows the E_{cc} values as a function of the charge in the low detuned dot of qubit A (the charge in dot 4, the low detuned QD of qubit B, is exactly the same due to symmetry). The values are shown in three different geometries: linear with $d = 160$, linear with $d = 120$ nm, and $d = 120$ nm with $\alpha = \beta = 0.45\pi$. It is evident from Fig. 6 that in the weakly coupled $\alpha = \beta = 0.45\pi$ case, the E_{cc} values stay small even with very large charge distribution asymmetries. In order to achieve the gate operation time of for example 50 ns (meaning that it takes 50 ns to achieve the maximal Bell-state entanglement), a cross-capacitance energy of $E_{cc} = 41.36$ neV is required (see the inset in Fig. 6). In the $\alpha = \beta = 0$ case with $d = 120$ nm, this corresponds to the charge asymmetry $q_1 = 1.0161\ e$, and in the $d = 160$ case to $q_1 = 1.0257\ e$. In the weakly coupled $d = 120$, $\alpha = \beta = 0.45\pi$ case, a much larger asymmetry of $q_1 = 1.1203\ e$ is needed for the same operation.

In addition to the charge-noise-induced decoherence, large charge asymmetry can also cause problems in the form of the singlet charge-state leakage. If the singlet is detuned close to the (0,2) regime nonadiabatically, the leakage between (1,1) and (0,2) could hinder the gate operation [27]. We simulate a nonadiabatic detuning sweep to a charge state corresponding to the aforementioned gate operation of 50 ns using the Hubbard model (the parameters are fitted to the continuum model data). The two-qubit system is initiated in $|S(1,1)\rangle_A \otimes |S(1,1)\rangle_B$.

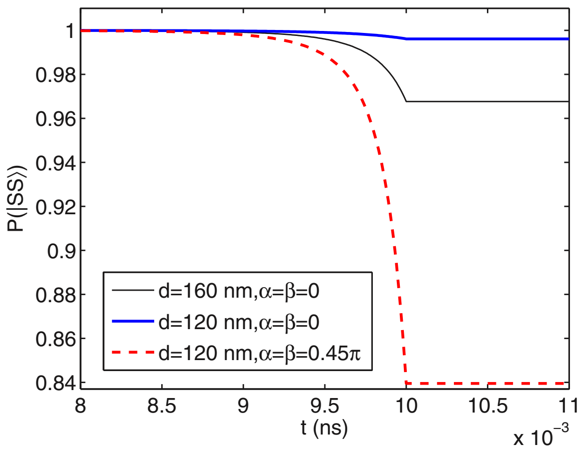

FIG. 7. (Color online) Occupation of the lowest $|SS\rangle$ state as a function of time. The two-qubit system is initiated in the $|S(1,1)\rangle_A \otimes |S(1,1)\rangle_B$ charge state. At $t = 0$ the detuning sweep is started. The detuning is increased to its maximum value ($\epsilon = 3.92$ meV in the $\alpha = \beta = 0$ case and $\epsilon = 4.25$ meV in the $\alpha = \beta = 0.45\pi$ case) that corresponds to a CPHASE operation with the duration of 50 ns. The detuning sweep's duration is $\tau = 0.01$ ns. At $t = 0.01$ ns, when the detunings have reached their final values, the system is let to evolve for 0.001 ns.

The detunings are then increased linearly to their maximum values ($\epsilon = 3.92$ meV in the $\alpha = \beta = 0$ case, $\epsilon = 4.22$ meV in the $d = 160$ nm case, and $\epsilon = 4.25$ meV in the $\alpha = \beta = 0.45\pi$ case) during a time of $\tau = 0.01$ ns. The occupations of the lowest $|SS\rangle$ and $|ST_0\rangle$ states are plotted as a functions of time in Fig. 7.

In the $d = 120$ nm and $\alpha = \beta = 0$ case, the singlet charge distribution corresponding to the 50 ns gate operation is very close to (1,1) ($q_1 = 1.0161\ e$), and thus the leakage from the lowest singlet state to the higher one is negligible. In Fig. 7, the occupations of the lowest $|SS\rangle$ and $|ST_0\rangle$ states are $P(|SS\rangle) = 0.996$ at the end of the detuning sweep. With $d = 160$ nm, the final occupation is $P(|SS\rangle) = 0.968$. In the $\alpha = \beta = 0.45\pi$ case, the final probability is $P(|SS\rangle) = 0.840$. The weaker coupling arising from the geometry of the two-qubit system and the consequent large charge asymmetries required for the gate operation result in probability leaking out of the qubit basis to higher singlet states if the detuning sweep is too fast. In this case, the gate cannot achieve maximal Bell-state entanglement [27] (the maximum concurrence is given by the final occupation of the lowest $|SS\rangle$ state). On the other hand, slow detuning pulses needed for an adiabatic passage to (0,2) could cause problems in controlling the qubits and their interaction. The nonadiabatic charge state leakage is discussed with more detail in our previous study [27].

Our analysis shows that the values of $E_{cc}^{\max}$ increase with decreasing qubit-qubit distance, and the largest values are obtained with trapezoidal dot formations, i.e., with the angles in Fig. 1 being $\alpha = -\beta$. The strongest coupling (with a given qubit-qubit distance) corresponds to a rectangular formation of the qubits ($\alpha = \pi/2$ and $\beta = -\pi/2$). In implementing the coupling scheme, systems of large $E_{cc}^{\max}$ values are preferable. Weak coupling arising from the geometry (long qubit-qubit distance or the "dead angles" cases) can cause problems for example in the form of charge-state leakage. It should be noted that the angle dependence of E_{cc} was found to be similar also with asymmetric detunings and with the closer dots 2 and 3 detuned to low potential (i.e., $\epsilon_A,\epsilon_B < 0$).

IV. SEVERAL QUBITS AND CLUSTER STATES

Bell states are created by applying a CPHASE gate between two capacitatively coupled $S - T_0$ qubits. By applying such gates between all adjacent pairs of an n-qubit array, a state belonging in the highly entangled class of cluster states is created. A cluster state corresponding to a certain array of qubits can be parametrized by a mathematical graph $G = (V,E)$, with the vertices V being the qubits and the edges E corresponding to their couplings [12]. Cluster states have applications for example in the proposed one-way quantum computing scheme where the system of qubits is first prepared into a cluster state and quantum computing algorithms are then implemented by measuring the qubits in a certain order and basis [15].

A general cluster state $|\phi_{N_q}\rangle$ of N_q $S - T_0$ qubits can be written as

$$|\phi_{N_q}\rangle = \frac{1}{2^{N_q/2}} \bigotimes_{k=1}^{N_q} \left(|S\rangle_k \sigma_z^{k+1} + |T_0\rangle_k\right), \tag{9}$$

where the subscript k corresponds to the qubit number k, and σ_z^{k+1} is the z Pauli matrix, (here, $\sigma_z^{N_q+1} = 1$). In the two-qubit case, $|\phi_2\rangle = \frac{1}{4}(|SS\rangle - |ST_0\rangle + |T_0S\rangle + |T_0T_0\rangle)$, a state which is equivalent to the maximally entangled Bell states $|\Psi_\pm\rangle = \frac{1}{\sqrt{2}}(|SS\rangle \pm |T_0T_0\rangle)$ up to local unitary transformations. Similarly, $|\phi_3\rangle$ is equivalent to the maximally entangled three-qubit Greenberger-Horne-Zeilinger (GHZ) states [9] $|GHZ_\pm\rangle = \frac{1}{\sqrt{2}}(|SSS\rangle \pm |T_0T_0T_0\rangle)$. However, with $N_q \geqslant 4$, the corresponding cluster states are not equal to the GHZ states [12].

In generating cluster states, the CPHASE operations between qubits can in principle be applied in an arbitrary order, simultaneously or in sequences [12,13,15]. In Ref. [30], we proposed a three-qubit gate for the creation of the three-qubit cluster state (or the GHZ state) in which the gate operation consists of just one step, setting all three qubits to the desired detuning values. In this scheme, the qubits were placed symmetrically in a triangular formation. In this section, we simulate the generation of GHZ states in several other three-qubit geometries. The following subsections concentrate in detail to two different qubit geometries that we use to demonstrate both the sequential on and one-step preparation of cluster states.

We simulate three qubits A (consisting of dots 1 and 2), B (dots 3 and 4), and C (dots 5 and 6), with the intraqubit dot distances being 80 nm and the qubit-qubit distances 120 nm. The confinement strength is $\hbar\omega_0 = 4$ meV. The detunings are defined as $\epsilon_A = V(\mathbf{R}_2) - V(\mathbf{R}_1)$, $\epsilon_B = V(\mathbf{R}_4) - V(\mathbf{R}_3)$, and $\epsilon_C = V(\mathbf{R}_5) - V(\mathbf{R}_6)$. The simulations are done using the extended Hubbard model of Eq. (3). The parameters of the model ($t_{ij} = 27.8\ \mu$eV, $U = 3.472$ meV, and $\eta = 0.43$ nm) are fitted to the two-qubit continuum model data with the same dot distances. We characterize the entanglement in three-qubit states using the pairwise concurrences and the three-tangle [11]

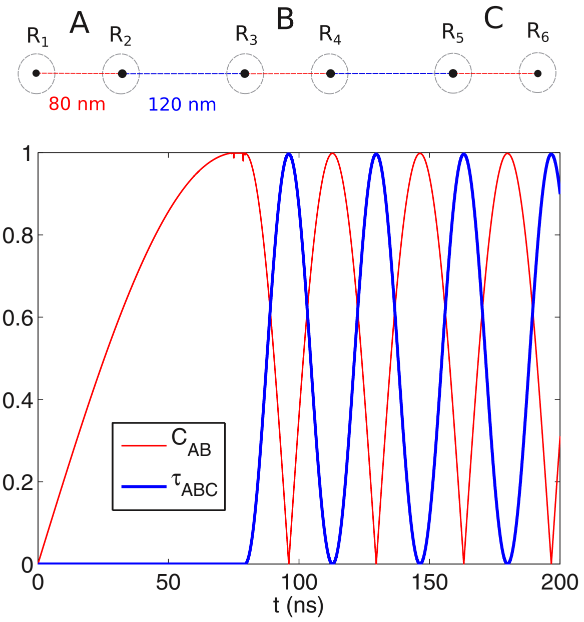

FIG. 8. (Color online) Evolution of the concurrences in a three-qubit system in the linear alignment geometry shown above the plot. The thick line shows the three-tangle τ_{ABC} and the thin line the pairwise concurrence of qubits A and B, C_{AB}. The qubits A, B, and C are initiated in the state $\frac{1}{\sqrt{2}}(|S\rangle + |T_0\rangle)$ with the detunings $\epsilon_A = -\epsilon_B = 4.0$ meV and $\epsilon_C = 0$. When C_{AB} has reached the maximum value 1 at $t = 76$ ns, the detunings ϵ_A and ϵ_B are decreased to zero, after which ϵ_B and ϵ_C are increased to the values 4.1 meV and −4.1 meV, respectively (the detuning sweeps are adiabatic with respect to the charge-state transition, lasting 2.5 ns). The system is then let to evolve for 200 ns.

that are computed at each time step as the system is evolved (the six-electron wave function is projected onto the three-qubit computational basis, and the concurrences are computed as in [11]). The time evolution of the six-electron wave function, $|\Psi(t)\rangle$, is computed by propagation with the Hubbard Hamiltonian of Eq. (3), $|\Psi(t + \Delta t)\rangle = \exp[-i\Delta t H(t)/\hbar]|\Psi(t)\rangle$.

A. Linear alignment and sequential preparation

In the linear alignment case (see the illustration in Fig. 8), the Coulomb repulsion between the qubits affects the middle qubit B differently compared to A and C. This asymmetry between the qubits makes it difficult to set the detunings of the qubits so that the Coulomb repulsion between them is symmetric. With significantly asymmetric repulsion, entangling the three qubits in a single step is not viable, as the entanglement oscillates very irregularly in this case (see the asymmetry discussions in Ref. [30]). Instead, we simulate a more general scheme in principle applicable to any array of $S - T_0$ qubits in which the interactions between qubits are turned on sequentially.

The evolution of the concurrences during the three-qubit operation are shown in Fig. 8. All three qubits A, B, and C are first initiated in the state $\frac{1}{\sqrt{2}}(|S\rangle + |T_0\rangle)$. Qubits A and B are then evolved under exchange with the detunings $\epsilon_A = -\epsilon_B = 4.0$ meV. The pairwise concurrence C_{AB} of A and B is computed, and when it reaches the maximal value $C_{AB} = 1$, i.e., when A and B are maximally entangled, the detunings ϵ_A and ϵ_B are decreased to zero adiabatically. Qubits B and C are then detuned to the values $\epsilon_B = 4.1$ meV and $\epsilon_C = -4.1$ meV adiabatically (i.e., in this pairwise operation, the farthest away dots are again detuned to low potential). When the detunings have reached their maximal values, the system is let to evolve for 200 ns.

As the qubits A and B are evolved under exchange, they start to entangle, as seen in the increasing values of C_{AB} in the figure. Switching off the detunings of A and B when their subsystem has reached the maximal Bell-state entanglement, and subsequently evolving B and C under exchange, results in true three-qubit entanglement. The system starts to oscillate between a GHZ state ($\tau_{ABC} = 1$, for example at $t = 96$ ns) and a Bell state between qubits A and B ($C_{AB} = 1$). The pairwise concurrences C_{BC} and C_{AC} stay approximately zero in this case; the entanglement in the system is either of the GHZ type between all three qubits or between just A and B.

The frequency of the oscillations is given by the value of E_{cc} similarly to Eq. (7) in the two subsystems (this also applies to the frequency of τ_{ABC} oscillations although their functional form is different). In Fig. 8, B and C are detuned to higher values, resulting in a larger value of E_{cc} and faster oscillations compared to the beginning of the simulation.

If the detunings of A and B are switched off before (or after) the maximal Bell-state peak, and B and C then detuned to exchange, also C_{BC} achieves nonzero values. In this case, τ_{ABC} never reaches 1, and the entanglement oscillates between C_{AB} and C_{BC}. For example, if the switch-off is done at $C_{AB} = 0.7$, both C_{AB} and C_{BC} oscillate between 0 and 0.7, while τ_{ABC} assumes values between 0 and 0.49.

The linear system was also studied with other qubit-qubit distances including asymmetric cases where the distance of A and B is different from the distance of B and C. The results were qualitatively similar to the ones already discussed. The geometry of the three-qubit system defines the E_{cc} values for the pairwise qubit couplings, which in turn determine the frequencies of the entanglement oscillations. Generally, the results discussed in Sec. III are directly applicable to the sequential entanglement scheme of arbitrary number of qubits, as in this case the entanglement is generated using only two-qubit CPHASE operations.

B. Parallel alignment and one-step preparation

In the parallel alignment geometry (the illustration of the geometry is seen in Fig. 9), the sequential coupling scheme works similarly to that in the linear case discussed in the previous section. The frequencies of the entanglement oscillations are again determined by the pairwise E_{cc} values. As the pairwise couplings are now of the rectangular type; stronger couplings are achieved compared to the linear case, as can be seen in Fig. 3. The qualitative features of the entanglement oscillations in the sequential scheme remain unchanged from the ones in Fig. 8.

Although the Coulomb repulsion between the three qubits is still not symmetrical in the parallel formation, the differences between qubits are smaller than in the linear case. This allows the generation of GHZ states using a single detuning pulse applied simultaneously to all three qubits, as in Ref. [30]. In

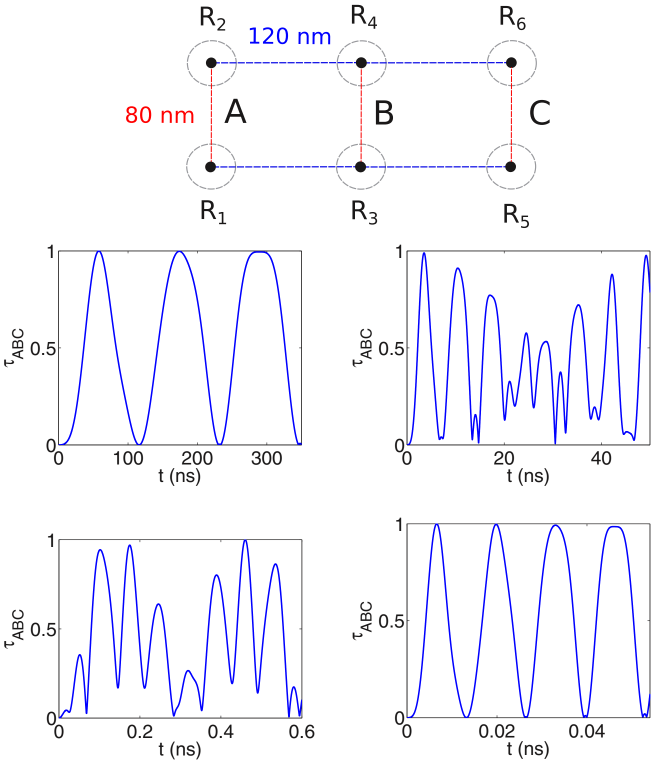

FIG. 9. (Color online) The evolution of the three-tangle with different detunings $\epsilon_A = \epsilon_B = \epsilon_C = \epsilon$ in the parallelly aligned case (the geometry is illustrated above the plots). At $t = 0$, all qubits are initiated in the xy plane of the Bloch sphere. The qubits are then let to evolve, and the concurrences and the three-tangle are computed at each time step. The upper left plot corresponds to $\epsilon = 4.5$ meV, the upper right to $\epsilon = 4.7$ meV, the lower left to $\epsilon = 4.9$ meV, and the lower right to $\epsilon = 5.6$ meV.

this case, all qubits are again initiated in the xy plane with the detunings $\epsilon_A = \epsilon_B = \epsilon_C = \epsilon$. The system is then evolved with these constant detunings causing the qubits to entangle with each other. Figure 9 shows the tangle evolution with different detunings ϵ.

The value of the detunings, ϵ, has a large qualitative effect on the τ_{ABC} oscillations. When ϵ is below or above the anticrossing region of the singlet charge states (i.e., $\epsilon < 4.6$ meV or $\epsilon > 5.5$ meV), τ_{ABC} oscillates between 0 and 1 with an approximately constant frequency. As seen in the upper left and lower right plots of Fig. 9, the wave form is still not completely periodic due to the aforementioned asymmetry between the qubits. When the detuning is in the anticrossing region (upper right and lower left plots in Fig. 9), the oscillations are more complex with modulation-like behavior. Apart from the small asymmetry effects, the qualitative features of the tangle oscillations are similar to the symmetric triangular case of Ref. [30], in which the behavior of the oscillations with different detunings is also discussed with more detail.

The one-step preparation scheme depends in a more complex manner on the geometry of the $S - T_0$ qubit system than the sequential one. It could in principle be used in the linear geometry of Fig. 8 as well, by again setting the detunings to $\epsilon_A = \epsilon_B = \epsilon_C = \epsilon$ and letting the system evolve.

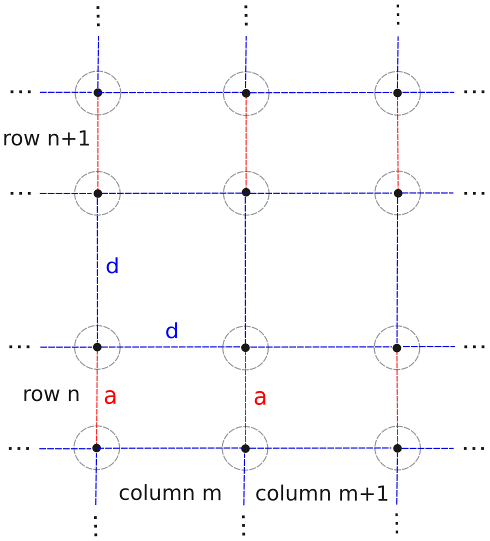

FIG. 10. (Color online) A two-dimensional $S - T_0$ qubit array. The intraqubit dot distances are a and the qubit-qubit distances d. The array is divided into N rows and M arrays. In each row, the qubits are coupled parallelly and in each column linearly.

However, in this case, it is found to result in very irregular entanglement oscillations that would be ill-suited for the experimental creation of cluster states. The reason for this difference between the two geometries is that in the linear geometry, the effect of the repulsion by the two other qubits depends heavily on the qubit in question. For example, the repulsion by A and B pushes the charge in C towards dot 6, in this case effectively lowering the E_{cc} value between qubits B and C. On the other hand, the repulsion by B and C enhances the E_{cc} value of A and B by pushing the charge in A into dot 1. In the parallel geometry, the interqubit repulsion acts by inhibiting the transition to (0,2). Although the system is still not symmetric between the three qubits, the aforementioned effect is larger in B than in A and C; the effects of the asymmetry are much smaller than in the linear case.

C. General case and qubit arrays

Finally, we will briefly discuss the creation of general cluster states between $S - T_0$ qubits. The generation of three-qubit GHZ states was also studied with other intraqubit orientations and distances, and the sequential entangling scheme was found to work similarly to the linear case in all studied geometries. In some sense, the parallel case discussed in the previous section can be considered to be the optimal geometry as it has the largest qubit-qubit couplings. The Coulomb-repulsion asymmetry between the qubits is also quite small in this formation.

Extending the sequential entanglement scheme beyond three qubits (i.e., adding more qubits to the formations in Figs. 8 and 9) results in an 1D array of qubits with a corresponding cluster state. Coupling several of such 1D arrays with each other then allows the creation of general graph states. Figure 10 shows an illustration of a 2D array of $S - T_0$ qubits. In the figure, the 2D array is divided into N rows and M

columns. In each row, the qubits are coupled parallelly and in each column linearly.

In the array geometry of Fig. 10, it should in principle be possible to entangle all qubits in a single row into cluster state with one single detuning pulse (similarly as in Fig. 9). The neighboring rows can then be entangled with each other again sequentially in one step per a pair of rows. Entangling the rows with each other should not affect the entanglement inside rows as the detuning values required for large E_{cc} values in the linear and parallel alignments differ considerably (see Fig. 3). The total number of entangling steps for obtaining a cluster state spanning the whole array is thus $M+1$. A cluster state corresponding to a given graph in the array can then be created by measuring the qubits that do not belong to the graph in the σ_z basis, which effectively removes them from the cluster [15].

In reality, however, fabricating perfectly symmetrical qubit arrays is impossible. The asymmetries in the array probably inhibit the one-step preparation of cluster states for entire rows of qubits. Instead, the preparation has to be done one qubit pair at a time, or at least between row and column segments instead of whole rows and columns. There are also many other experimental limitations, including how the electrostatic gating defining the quantum dot potentials should be conducted in such arrays. The experimental issues are however outside the scope of this paper and the analysis in this section should be considered a preliminary study on many-qubit arrays and cluster states in the $S-T_0$ qubit architecture.

V. DISCUSSION

Using exact diagonalization techniques, we have first computed the energy eigenstates of a two-qubit system with several different qubit-qubit distances and discussed their effect on the capacitative coupling of the two qubits. Longer qubit-qubit distances were found to result in weaker coupling due to smaller differences in the Coulomb repulsion between the qubit states. The effect of the orientation of the qubits with respect to each other was also discussed. We find that the coupling is strong with short qubit-qubit distances, and trapezoidal dot formations. These geometries are preferable in creating efficient two-qubit gates. They allow smaller localization of the singlet electrons in the gate operation, which in turn decreases the charge-based decoherence and charge-state leakage between $S(1,1)$ and $S(0,2)$.

We also discussed the creation of cluster states and multiqubit entanglement using the capacitative coupling. Several interqubit geometries were studied. We simulated the creation of a three-qubit cluster states using the extended Hubbard model with its parameters fitted to continuum model data. We simulated both the simultaneous and pairwise detuning schemes for the creation of three-qubit entanglement. We also discussed the creation of cluster states corresponding to large qubit arrays and arbitrary graphs.

In this paper, we have not modeled the decoherence effects explicitly. Of the different sources of decoherence, the charge noise is possibly the most severe in the case of the capacitative coupling. The faster the gate operation, i.e., the larger the differences in the singlet and triplet charge distributions, the more susceptible the system is to charge noise [22,24,25,29]. The ability to increase the qubit-qubit coupling without increasing the charge distribution differences is thus on demand. Another important source of decoherence is the semiconductor nuclear spin bath [18,19]. It is however suppressed during the capacitative coupling operation due to the significant exchange energy in the qubits [4,31,32].

In conclusion, we have studied the capacitative coupling of singlet-triplet qubits using exact diagonalization techniques. Our analysis on the geometry of the two-qubit system and its effect on the coupling strength can be used to aid experimentalists in creating efficient realizations of the capacitative coupling scheme. The geometries allowing stronger couplings can be used to alleviate the decoherence problem, and we see no reasons that would prevent their use in implementing the coupling scheme experimentally. The analysis was also extended to three qubits, and the scheme for the creation of highly entangled cluster states should in principle be applicable to any number of singlet-triplet qubits.

ACKNOWLEDGMENTS

We acknowledge support from Academy of Finland through its Centers of Excellence Program (Project No. 251748).

---

[1] D. Loss and D. P. DiVincenzo, Phys. Rev. A **57**, 120 (1998).

[2] J. Levy, Phys. Rev. Lett. **89**, 147902 (2002).

[3] J. Taylor, H. Engel, W. Dür, A. Yacoby, C. Marcus, P. Zoller, and M. Lukin, Nat. Phys. **1**, 177 (2005).

[4] J. Petta, A. Johnson, J. Taylor, E. Laird, A. Yacoby, M. Lukin, C. Marcus, M. Hanson, and A. Gossard, Science **309**, 2180 (2005).

[5] S. Foletti, H. Bluhm, D. Mahalu, V. Umansky, and A. Yacoby, Nat. Phys. **5**, 903 (2009).

[6] M. Shulman, O. Dial, S. Harvey, H. Bluhm, V. Umansky, and A. Yacoby, Science **336**, 202 (2012).

[7] D. Stepanenko and G. Burkard, Phys. Rev. B **75**, 085324 (2007).

[8] R. Horodecki, P. Horodecki, M. Horodecki, and K. Horodecki, Rev. Mod. Phys. **81**, 865 (2009).

[9] D. M. Greenberger, M. A. Horne, A. Shimony, and A. Zeilinger, Am. J. Phys. **58**, 1131 (1990).

[10] W. Dür, G. Vidal, and J. I. Cirac, Phys. Rev. A **62**, 062314 (2000).

[11] V. Coffman, J. Kundu, and W. K. Wootters, Phys. Rev. A **61**, 052306 (2000).

[12] H. J. Briegel and R. Raussendorf, Phys. Rev. Lett. **86**, 910 (2001).

[13] M. Borhani and D. Loss, Phys. Rev. A **71**, 034308 (2005).

[14] R. Raussendorf and H. J. Briegel, Phys. Rev. Lett. **86**, 5188 (2001).

[15] R. Raussendorf, D. E. Browne, and H. J. Briegel, Phys. Rev. A **68**, 022312 (2003).

[16] A. Barenco, C. H. Bennett, R. Cleve, D. P. DiVincenzo, N. Margolus, P. Shor, T. Sleator, J. A. Smolin, and H. Weinfurter, Phys. Rev. A **52**, 3457 (1995).

[17] A. Johnson, J. Petta, J. Taylor, A. Yacoby, M. Lukin, C. Marcus, M. Hanson, and A. Gossard, Nature (London) **435**, 925 (2005).

[18] F. H. L. Koppens, J. A. Folk, J. M. Elzerman, R. Hanson, L. H. W. van Beveren, I. T. Vink, H. P. Tranitz, W. Wegscheider, L. P. Kouwenhoven, and L. M. K. Vandersypen, Science **309**, 1346 (2005).

[19] A. V. Khaetskii, D. Loss, and L. Glazman, Phys. Rev. Lett. **88**, 186802 (2002).

[20] I. A. Merkulov, A. L. Efros, and M. Rosen, Phys. Rev. B **65**, 205309 (2002).

[21] X. Hu and S. Das Sarma, Phys. Rev. Lett. **96**, 100501 (2006).

[22] O. E. Dial, M. D. Shulman, S. P. Harvey, H. Bluhm, V. Umansky, and A. Yacoby, Phys. Rev. Lett. **110**, 146804 (2013).

[23] I. van Weperen, B. D. Armstrong, E. A. Laird, J. Medford, C. M. Marcus, M. P. Hanson, and A. C. Gossard, Phys. Rev. Lett. **107**, 030506 (2011).

[24] G. Ramon and X. Hu, Phys. Rev. B **81**, 045304 (2010).

[25] G. Ramon, Phys. Rev. B **84**, 155329 (2011).

[26] E. Nielsen, R. W. Young, R. P. Muller, and M. S. Carroll, Phys. Rev. B **82**, 075319 (2010).

[27] T. Hiltunen, J. Ritala, T. Siro, and A. Harju, New J. Phys. **15**, 103015 (2013).

[28] J. Nickolls, I. Buck, M. Garland, and K. Skadron, Queue **6**, 40 (2008).

[29] E. Nielsen, R. P. Muller, and M. S. Carroll, Phys. Rev. B **85**, 035319 (2012).

[30] T. Hiltunen and A. Harju, Phys. Rev. B **89**, 115322 (2014).

[31] W. A. Coish and D. Loss, Phys. Rev. B **72**, 125337 (2005).

[32] J. Särkkä and A. Harju, Phys. Rev. B **77**, 245315 (2008).